

CHARACTERIZATION OF HYDROGENATED AMORPHOUS SILICON
USING THE CONSTANT PHOTOCURRENT METHOD

by

JIN MIAO SHEN, B.S.

A THESIS

IN

PHYSICS

Submitted to the Graduate Faculty
of Texas Tech University in
Partial Fulfillment of
the Requirements for
the Degree of

MASTER OF SCIENCE

Approved

Accepted

August, 1992

805
T3
1992
No. 100
Cop. 2

ACKNOWLEDGEMENTS

PKC
AEA 8974
JAC 4/3/93

I would like to take this opportunity to thank my adviser Dr. Shubhra Gangopadhyay for her keen supervision, patient guidance throughout the course of the study. I am thankful to Dr. Roger L. Lichti and Dr. C. David Lamp for agreeing to serve on my thesis committee and for their valuable advice. I am also grateful to my friend, C. Palsule, for his helpful suggestions and discussions. Finally, I wish to dedicate this work to my wife.

TABLE OF CONTENTS

ACKNOWLEDGEMENTS	ii
ABSTRACT	iv
LIST OF TABLES	v
LIST OF FIGURES	vi
CHAPTER	
1. INTRODUCTION	1
2. HYDROGENATED AMORPHOUS SILICON (a-Si:H)	
2.1 Structure and Electronic Features of a-Si:H	4
2.2 The Optical Absorption Edge of a-Si:H	9
2.3 Light-induced Metastable Defects in a-Si:H	14
3. THEORY OF THE CONSTANT PHOTOCURRENT METHOD (C.P.M.)	19
4. EXPERIMENTAL SET-UP	24
5. RESULTS AND DISCUSSION	28
6. CONCLUSIONS	42
REFERENCES	45
APPENDIX	47

ABSTRACT

The objective of this work is to study the electrical and optical properties of hydrogenated amorphous silicon using the constant photocurrent method (CPM). The absorption coefficients have been obtained for both undoped and phosphorus-doped a-Si:H films. The CPM spectrum has been compared with the absorption spectrum obtained from photothermal deflection spectroscopy. Some important parameters, such as the Urbach energy, optical gap, and defect density, have been obtained from the CPM spectrum. The light induced creation of defects has been investigated for different exposure times at 100 mW/cm² illumination intensity. These light induced defects can be annealed out by heating the sample to above 150 - 200°C. The experimental data agree with the bond breaking model. According to this model, the weak Si-Si bonds in the matrix are broken, or altered, followed by local atomic rearrangement into metastable equilibrium.

LIST OF TABLES

4.1 Sample specifications.	27
5.1 Optical gap and Urbach energy of sample A and sample B.	33
5.2 Defect densities of sample A and sample B.	36
5.3 Defect densities of sample A for different exposure times.	37
5.4 Comparison of E_g , E_o , and N_s of initial state of sample A with those after 10 hr. exposure and 1hr. annealing.	41
A.1 Comparison of E_g , E_o , and N_s of initial state of sample A using CPM and PDS.	47
A.2 Comparison of E_g , E_g , and N_s of initial state of sample B using CPM and PDS.	47

LIST O FIGURES

2.1	Schematic of a continuous random network containing atoms of different bonding coordination.	5
2.2	Schematic of electron diffraction on crystalline and amorphous silicon.	6
2.3	Schematic of density of states for a-Si:H.	8
2.4	Schematic of absorption edge of a-Si:H.	10
2.5	Illustration of "excess absorption" represented by the shaded portion.	13
2.6	Illustration of the potential well model.	16
2.7	Schematic of the recombination model used to explain the creation of defects by illumination.	18
3.1	Illustration of possible transitions in undoped a-Si:H.	22
4.1	Schematic of CPM experimental set up.	25
5.1	Absorption spectrum of sample A using CPM.	29
5.2	Absorption spectrum of sample B using CPM.	30
5.3	Square root of αE versus photon energy E for sample A.	31
5.4	Square root of αE versus photon energy E for sample B.	32
5.5	Comparison of absorption spectra of sample A using CPM and PDS.	34
5.6	Absorption spectra of sample A after different exposure times to $100 \text{ mW}(\text{cm})^{-2}$.	38
5.7	Comparison of absorption spectra of sample A after 1 hr. annealing at 200°C in dark and after 10 hr. exposure to $100 \text{ mW}(\text{cm})^{-2}$.	40

CHAPTER 1

INTRODUCTION

During the past twenty years the subject of amorphous semiconductors has progressed from almost total obscurity to attainment of device structures, such as solar cells, flat panel displays and optical memories that are now commercially available. Among them, ^[hai'dro'dzineitið]hydrogenated amorphous silicon (a-Si:H) has attractive properties such as continuously adjustable band gap, a usable carrier lifetime, efficient optical transitions, and capability of employing either type of dopants. In addition to these properties, hydrogenated amorphous silicon can be fabricated very easily as a thin film by a technology which is considerably cheaper and less sophisticated than the one required for crystalline silicon. As a result, hydrogenated amorphous silicon has been used for very large scale applications such as solar panels for irrigation and remote electrification.

On the other hand, the amorphous silicon has a "depressing" property: light induced ^{光诱导}metastability. ^{亚稳态}The metastability is that its electronic structure and defect density will change under prolonged illumination or heating at high temperature. Because of inadequate understanding of the electronic phenomena in amorphous silicon materials, it still hampers the solution of this problem and still imposes severe limitations for device purposes in many application fields.

The important difference between crystalline and amorphous semiconductors is that the amorphous semiconductors have short-range order and lack long-range order in their structures. The structural disorder influences the electronic properties in several different ways. The similarity of the covalent silicon bonds in crystalline and amorphous silicon leads to a similar overall electronic structure: amorphous and crystalline phases of the same material tend to have comparable band gaps. The disorder represented by deviations in the bond lengths and bond angles broadens the electron distribution of states and causes electron and hole localization. Structural defects, such as under or over coordinated atoms, strained bonds and impurities, have corresponding electronic states which lie in the band gap. The possibility of alternative bonding configurations of each atom leads to a strong interaction between the electronic and structural states and causes the phenomenon of metastability [1].

It should be emphasized that the structural defects with electronic states in band gap control the electronic transport and recombination properties. So, the defect density of states is important in determining the quality of the material. In hydrogenated amorphous silicon, for example, material with a gap-state defect density at or below 10^{16} cm^{-3} produces high efficiency solar cells, while performance is quite poor for

densities above $5 \times 10^{16} \text{ cm}^{-3}$ [2]. Thus accurate determination of the defect density is very critical.

Of the various experimental techniques for measuring the density of defect states in a-Si:H, optical absorption for photon energies less than the ^{band} mobility gap determined by constant photocurrent method (CPM) offers several advantages. First, it can be performed on both doped and undoped films. Second, it is only bulk sensitive in the region of low photon energy. Third, it is capable of measuring the absorption coefficient down to 10^{-2} cm^{-1} and provides a very sensitive measurement for films.

The objective of this work is to carry out absorption measurements on ^{intrinsic} and P-doped a-Si:H films for obtaining some important parameters such as optical band gap, Urbach energy, density of states, and to investigate the effects of light illumination and annealing on the defect density of states.

CHAPTER 2

HYDROGENATED AMORPHOUS SILICON

2.1 Structure and Electronic Features of a-Si:H

The lack of long range order is the main feature which distinguishes amorphous from crystalline materials. Generally, the structure of amorphous silicon can be classified into a continuous random network (CRN) appropriate to the structure of covalent type materials (Fig.2.1) [1]. In the CRN, the nearest neighbor separation and bond lengths are nearly equal to those in crystalline silicon. The bulk atomic structure of a-Si is such that on average a Si atom has four others around it at the same distance (as in a crystal) forming a regular tetrahedron. Each of these atoms in turn has three more neighbors, similarly arranged, giving rise to a well-defined second shell of 12 atoms, none of which is a neighbor to any other. The structural data show that the resemblance of a-Si to crystalline Si ceases beyond the second shell [3].

Experimentally, techniques such as X-ray diffraction or neutron diffraction can be used to quantitatively determine the absence of long-range order in a-Si:H. Figure 2.2 [4] shows the results of electron diffraction experiments on crystalline and amorphous silicon. From the figure, we can easily find that the well known structure of crystalline Si can be described as a central Si atom surrounded by four nearest neighboring Si atoms 2.35\AA away, forming a regular

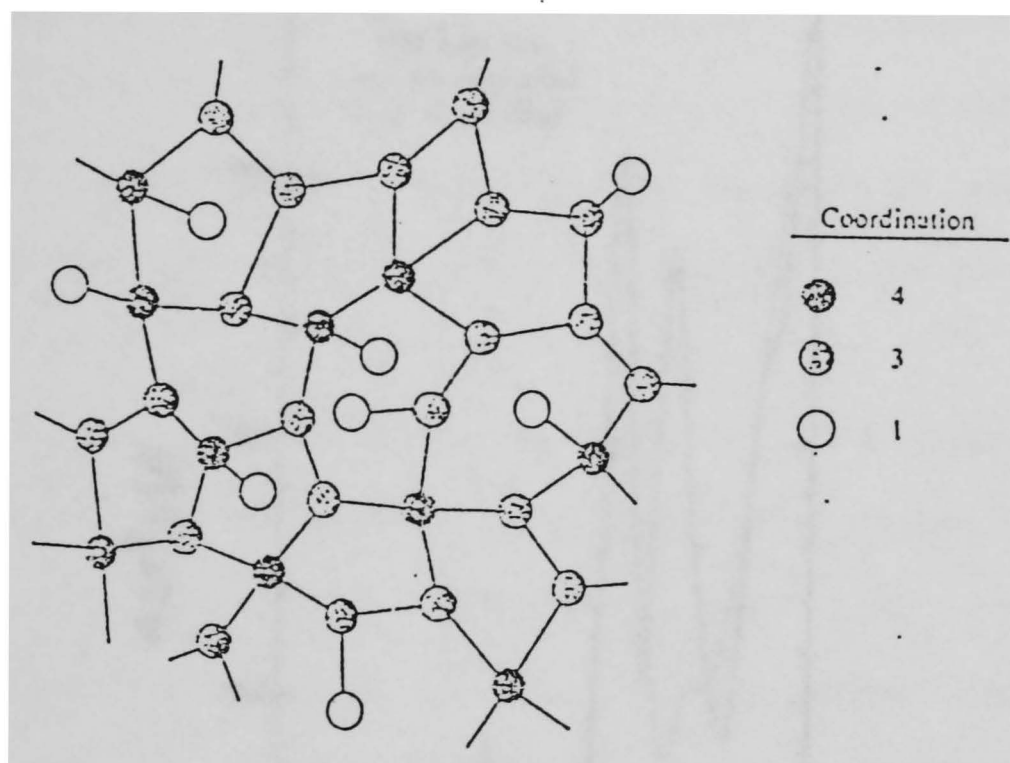


Figure 2.1
Schematic of a continuous random network containing
atoms of different bonding coordination.

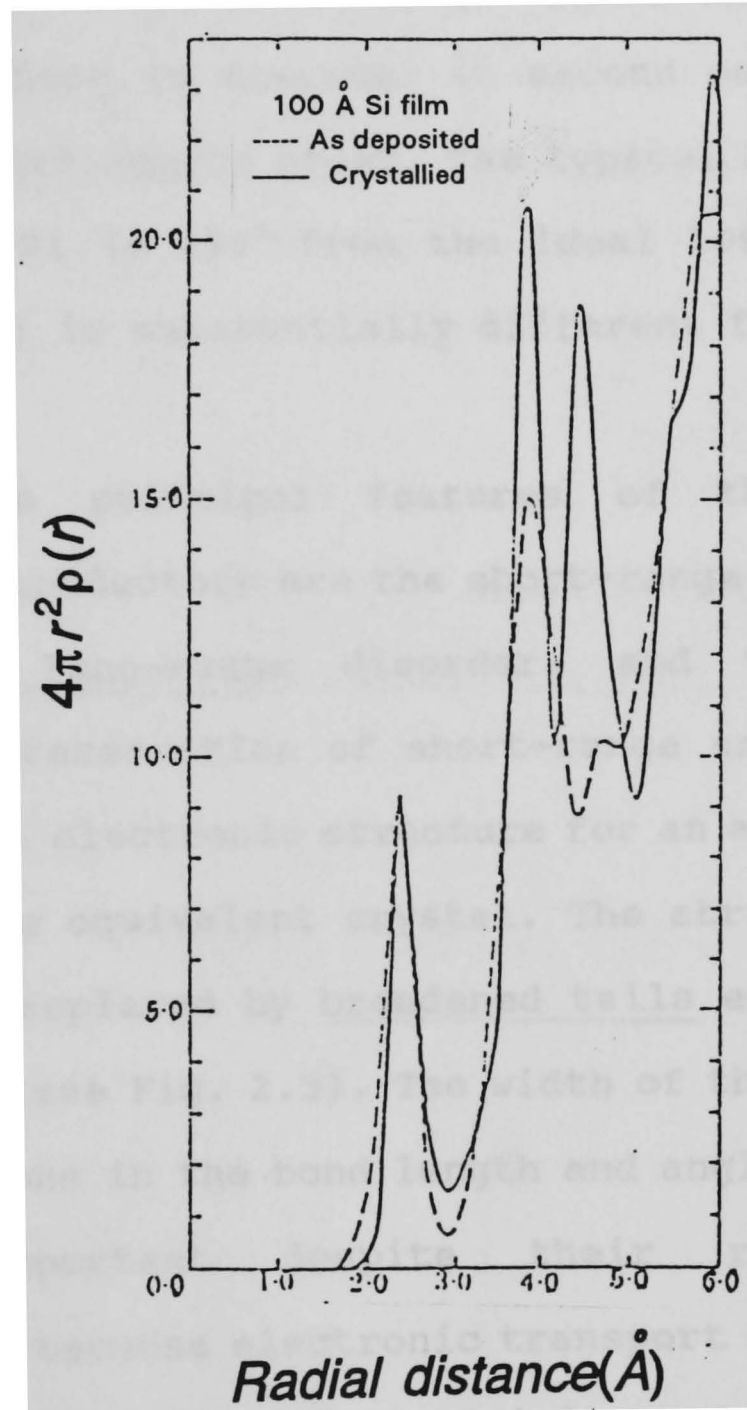


Figure 2.2 Schematic of electron diffraction on crystalline and amorphous silicon.

tetrahedron, and there is a second neighbor shell 3.84\AA away and third neighbor shell 4.5\AA away from the central atom. In the case of a-Si, the second neighbor peak itself is diffused and the third neighbor peak is almost undetectable. This clearly indicates that even though the nearest environment is tetrahedral, there is disorder in second neighbor shell and almost no dihedral-angle order. The typical bond-angle spread observed in a-Si is $\pm 10^\circ$ from the ideal 109.5° and dihedral angle (average) is substantially different from the ideal 60° [5].

The three principal features of the structure of amorphous semiconductors are the short-range order of an ideal network, the long-range disorder, and the coordination defects. The preservation of short-range order results in a similar overall electronic structure for an amorphous material compared to the equivalent crystal. The abrupt band edges of a crystal are replaced by broadened tails extending into the forbidden gap (see Fig. 2.3). The width of these tails depends on the deviations in the bond length and angle. The band tails are most important despite their relatively small concentration, because electronic transport occurs at the band edges. The coordination defects mainly produce dangling bonds [6], which are point defects introduced due to unsatisfied bonds of a tetravalently bonded silicon atom. The defects result in electronic states deep within the band gap. These defects determine many electronic properties by controlling

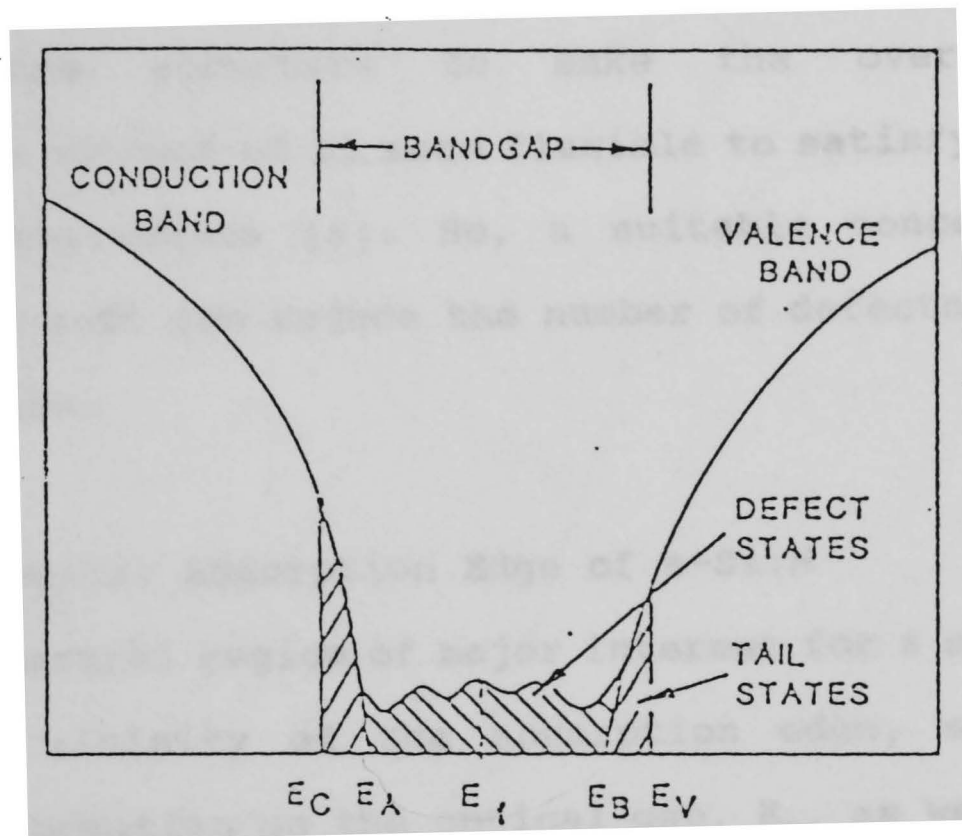


Figure 2.3

Schematic of density of states for a-Si:H.

trapping and recombination. With the addition of hydrogen, the density of localized states in the band gap decreases. This happens because the hydrogen passivates dangling bond states, usually by terminating silicon bonds. Furthermore, hydrogen modifies the structure to make the over-constrained tetrahedral network of Si more flexible to satisfy most of the bonding requirements [6]. So, a suitable concentration of hydrogen in a-Si can reduce the number of defects and improve its structure.

2.2 The Optical Absorption Edge of a-Si:H

The spectral region of major interest for a semiconductor is in the vicinity of the absorption edge, since it can provide information on the optical gap, E_g , as well as on the density of states within the gap. Although amorphous semiconductors synthesized under different conditions often exhibit large differences in their optical properties, there remains remarkable agreement in the shape of the optical absorption edge. It is widely accepted that the optical absorption curves of amorphous materials exhibit three distinct regions, as shown in the plot of optical absorption coefficient versus energy in Fig.2.4: a shoulder in the optical absorption (region A) for $\alpha \leq 1\text{cm}^{-1}$, an exponential rise (region B) for $1\text{ cm}^{-1} \leq \alpha \leq 10^3\text{cm}^{-1}$, and a slowly varying region (region C) for $\alpha \geq 10^4\text{ cm}^{-1}$.

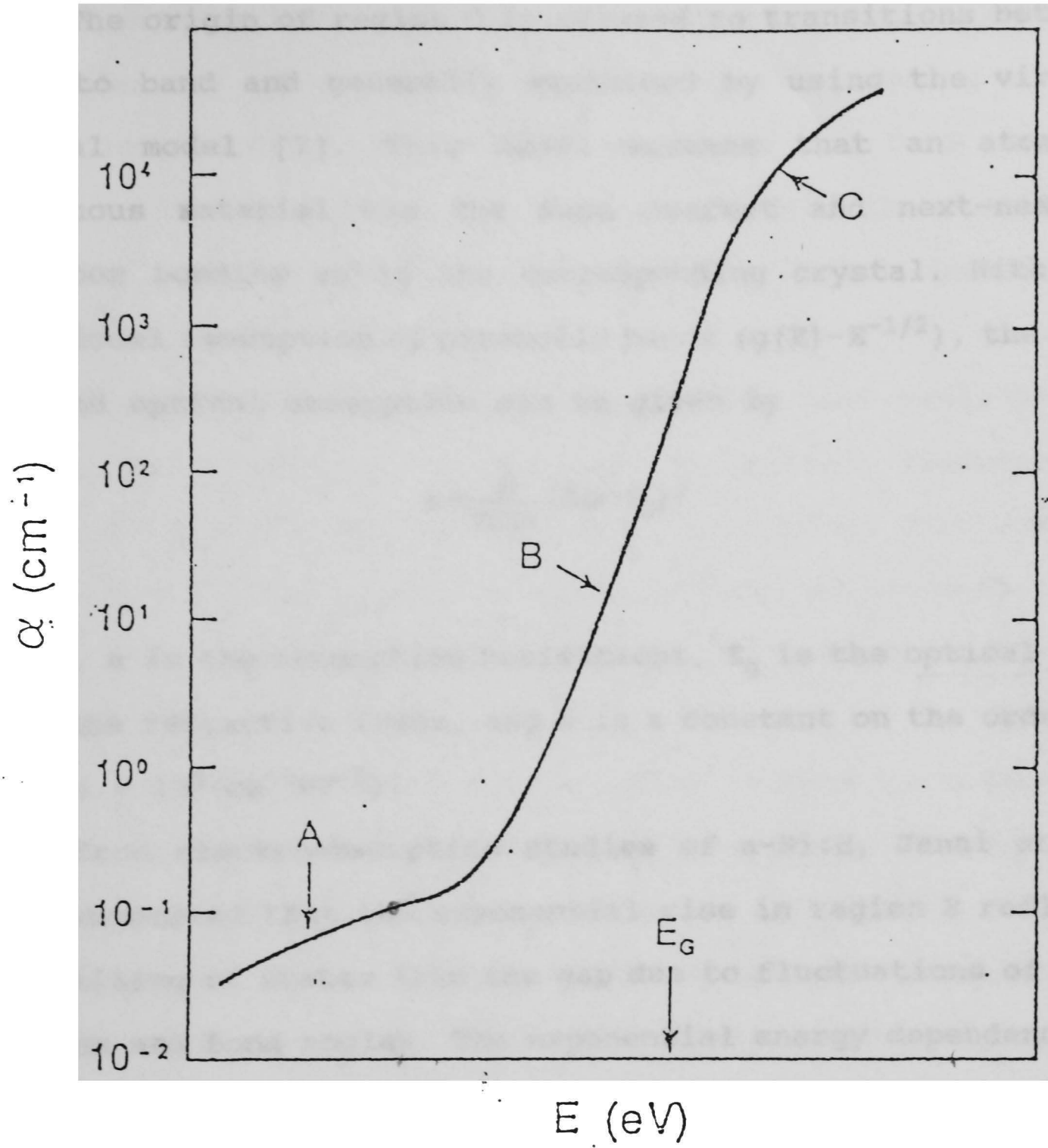


Figure 2.4

Schematic of absorption edge of a-Si:H.

The origin of region C is related to transitions between band to band and generally explained by using the virtual crystal model [7]. This model assumes that an atom in amorphous material has the same nearest and next-nearest neighbor bonding as in the corresponding crystal. With the additional assumption of parabolic bands ($g(E) \sim E^{-1/2}$), the band to band optical absorption can be given by

$$\alpha = \frac{B}{nh\omega} (h\omega - E_g)^2 \quad (1)$$

where, α is the absorption coefficient, E_g is the optical gap, n is the refractive index, and B is a constant on the order of 3 to $6 \times 10^5 (\text{cm}^{-1}\text{eV}^{-1})$.

From electroabsorption studies of a-Si:H, Janai et al. [8] suggested that the exponential rise in region B reflects the tailing of states into the gap due to fluctuations of bond lengths and bond angles. The exponential energy dependence of the absorption coefficient $\alpha(E)$ in region B can be expressed by [9]

$$\alpha(h\omega) = \alpha_o \text{EXP}\left(\frac{E - E_I}{E_o}\right) \quad (2)$$

where E_o is the slope of the exponential tail (also called Urbach energy), and E_I and α_o are an experimentally determined prefactors.

Generally, this region depends on the total (electron and hole) density of states and reflects the broadening of the bands due to deviations in bond lengths and bond angles. Commonly, the valence band tail is broader than the conduction band tail, and therefore dominates the total density of states.

In region A, the subgap absorption is most sensitive to preparation conditions, such as deposition temperature, substrate temperature, gas pressure, and doping. Furthermore, even after the deposition of the materials, exposure to light or high temperatures, will affect the subgap absorption significantly.

The origin of the subgap spectral feature is related to midgap defect states. The optical absorption arising from transitions involving defect states is weak due to the low defect densities as compared to the densities of conduction and valence band states. Optical transmission techniques can not be used in this region due to low sensitivity. Highly sensitive techniques for measuring low values of the absorption coefficient, such as Photoacoustic Spectroscopy (PAS), Photothermal Deflection Spectroscopy (PDS), and Constant Photocurrent Method (CPM), are used to provide information about the defect state density.

N.M.Amer et al. [10] postulated that with a constant optical matrix element, the integral of the ^{吸收}excess absorption ^{积分}in a-Si:H, beyond that identified with an extrapolated Urbach

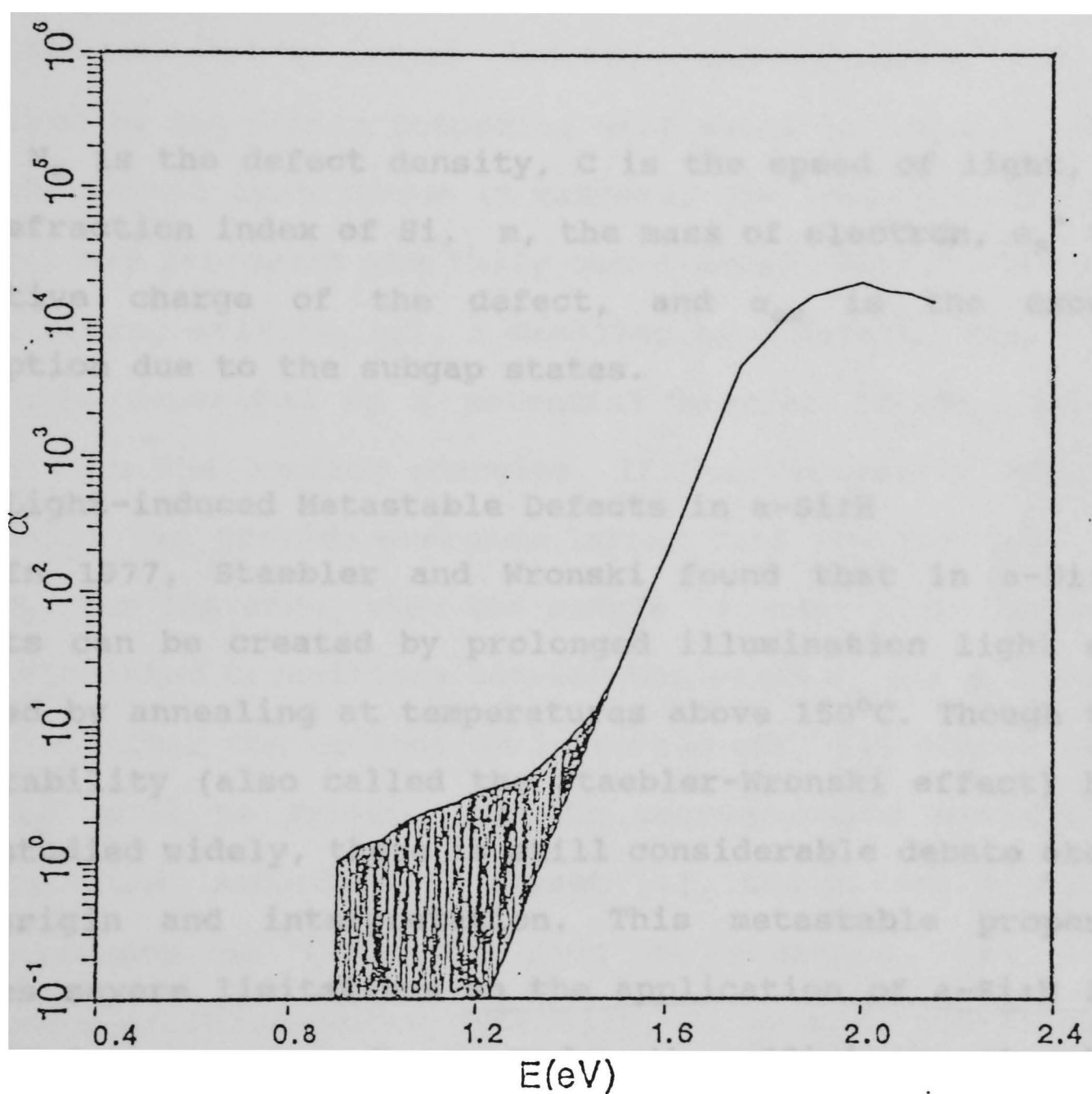


Figure 2.5
Illustration of "excess absorption" represented
by the shaded portion.

tail, should be proportional to the defect density. This "excess absorption" is described by the shaded portion in Figure 2.5. The density of defects can be calculated as

$$N_s = \frac{Cnm}{2\pi h^2 (e_s^*)^2} \int \alpha_{ex}(E) dE \approx 7.9 \times 10^{15} \int \alpha_{ex}(E) dE \quad (3)$$

where N_s is the defect density, C is the speed of light, n , the refraction index of Si, m , the mass of electron, e_s^* the effective charge of the defect, and α_{ex} is the excess absorption due to the subgap states.

2.3 Light-induced Metastable Defects in a-Si:H

In 1977, Staebler and Wronski found that in a-Si:H, defects can be created by prolonged illumination light and removed by annealing at temperatures above 150°C. Though the metastability (also called the Staebler-Wronski effect) has been studied widely, there is still considerable debate about its origin and interpretation. This metastable property imposes severe limitations on the application of a-Si:H for some device purposes. For example, the efficiency of solar cells decreases by the exposure of sunlight.

It is generally believed that the origin of the metastability is connected with the creation of bulk dangling bond defects. M. Stutzmann and W.B. Jackson used Electron Spin Resonance (ESR) and photoconductivity measurements to investigate the influence of many parameters, such as

illumination time, illumination intensity, annealing temperature, sample thickness, and impurity content on the metastability. They suggested that the metastable changes are due to the creation of dangling bonds resulting from breaking of weak Si-Si bonds [11].

The metastable defect creation and annealing can be described by the double potential well model in Fig.2.6 [12]. When the defect equilibrium is reached, the lower energy well (E_0, q_0) may represent the fully coordinated network, and the higher energy well (E_1, q_1), a dangling bond defect. These two wells are separated by a potential barrier ($V_0, \Delta q_0$) which arises from the bonding energies. If the externally applied excitation can provide energies larger than the barrier, $E_{ex} \geq \Delta E + V_0$, for instance, when the sample is under illumination, then stimulated transitions between the state q_0 and q_1 become possible. After the excitation is turned off, all states with $E \gg k_B T$ will be frozen into the corresponding metastable configuration. According to Street [1], the defect density, N_s , increases as the cube root of exposure time. The dependence on illumination intensity, G , is also non-linear, having a power close to 0.6 for the creation of metastable defects. Defect creation can thus be described by $N_s = \text{Const.} G^{0.46} t^{0.33}$. By annealing an illuminated sample at temperatures 150-200°C, the electronic properties of the sample can be restored. This can be explained as a relaxation into the equilibrium ground state q_0 in the potential well

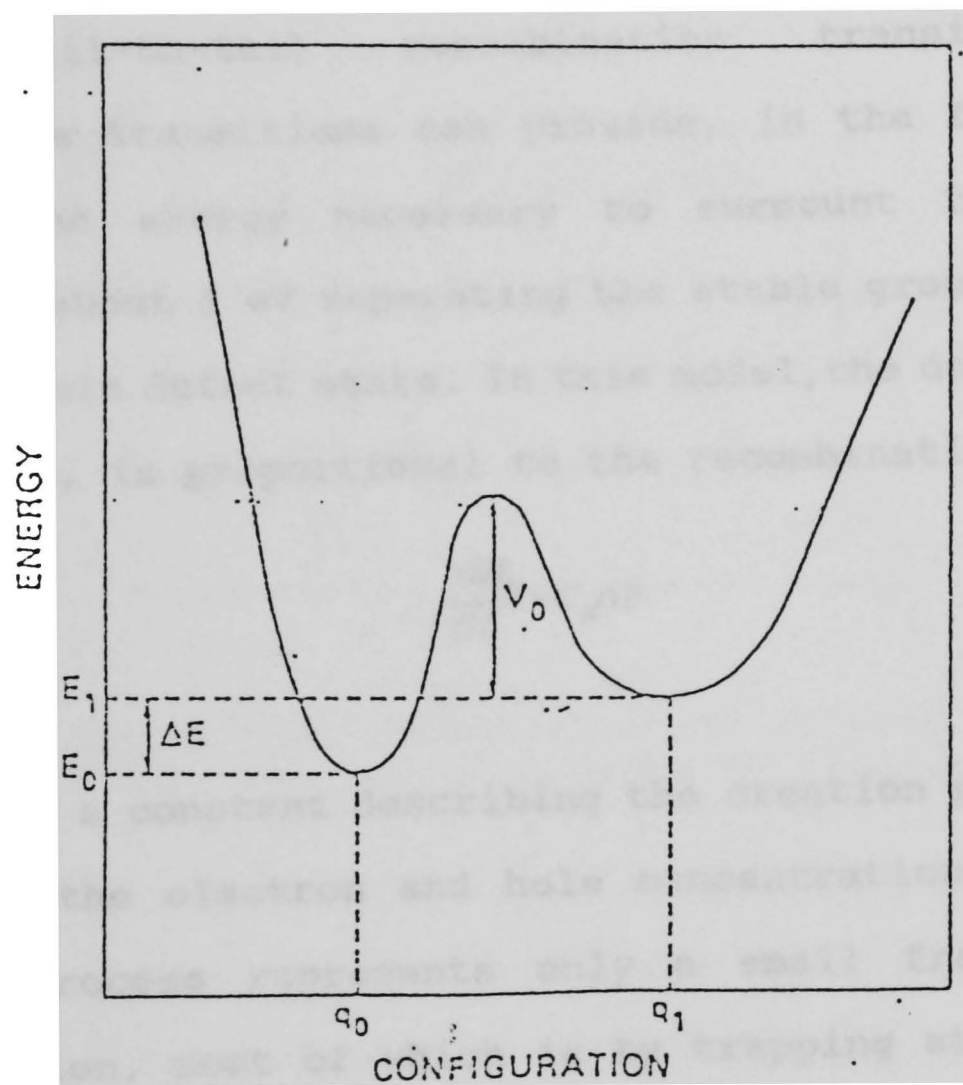


Figure 2.6

Illustration of the potential well model.

model by providing sufficient thermal energy to cross the barrier. The kinetics of defect creation can also be explained by the recombination model proposed by Stutzmann et al. in Fig.2.7 [11]. This model is based on the assumption that new metastable bonds are created by the fraction of nonradiative, direct tail-to-tail recombination transitions. The nonradiative transitions can provide, in the form of local phonons, the energy necessary to surmount the potential barrier of about 1 eV separating the stable ground state from the metastable defect state. In this model, the defect creation rate, dN/dt , is proportional to the recombination rate:

$$\frac{dN_D}{dt} = C_d n P \quad (4)$$

where C_d is a constant describing the creation probability, n and P are the electron and hole concentrations. The defect creation process represents only a small fraction of the recombination, most of which is by trapping at the dangling bond defects. So, the light induced effects are characterized by very slow creation.

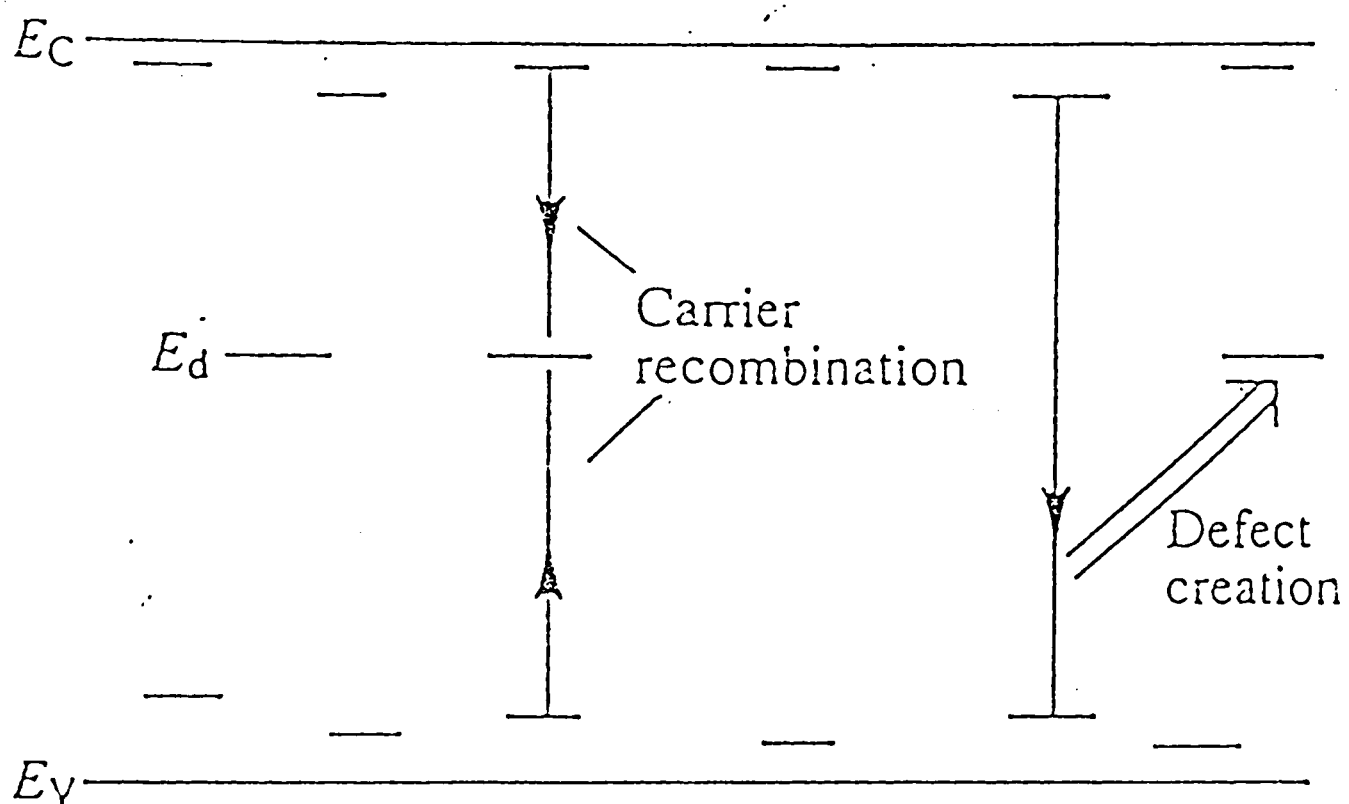


Figure 2.7
Schematic of the recombination model used to explain the creation of defects by illumination.

CHAPTER 3

THEORY OF THE CONSTANT PHOTOCURRENT METHOD

The constant photocurrent method (CPM) gives a direct measurement of band tail absorption. The method was invented by Grimmeiss and Ledebor [13] for measuring the spectral dependence of ion scattering cross sections of deep impurities in crystalline semiconductors and applied to the investigation of deep levels in GaAs.

Compared with other methods which measure absorption coefficient, such as Photoacoustic Spectroscopy (PAS), Photothermal Deflection Spectroscopy (PDS), the method of CPM has some attractive features. CPM is capable of measuring α down to values about 10^{-2}cm^{-1} and provides a very sensitive measure of absorption coefficient of thin films. The method is only bulk sensitive in the range, $\alpha d \ll 1$. The basic idea of CPM is that, If the photocurrent is kept constant, then recombination mechanism is unchanged, and response time and recombination life is not a function of energy.

Generally, photocurrent is influenced by the sample and illumination geometry and the kind of electrical contacts [14]. When ohmic contacts are used, for instance, coplanar contacts in a-Si:H samples, the photocurrent measured is the secondary photocurrent ($I_{s,ph}$). The secondary photocurrent can result from electrons, holes or both of them. If blocking contacts are used the photocurrent, called the primary

photocurrent ($I_{p,ph}$), can flow only if both electrons and holes are extracted. 光生電流

The electron part of the secondary photocurrent is given by

$$I_{s,ph} \approx eN(1-R) [1 - \exp(-\alpha d)] \mu_0 \tau_1 \eta F \quad (5)$$

where e is the electron charge, N is the number of incident photons, η is the quantum efficiency, τ_1 is the free carrier lifetime, μ_0 is the free carrier mobility, and F is the applied electric field. $N(1-R)[1 - \exp(-\alpha d)]$ is the number of photons absorbed in the sample with reflection coefficient R , absorption coefficient α , and sample thickness d .

If $\alpha d \ll 1$, equation (5) can be simplified to

$$I_{s,ph} \approx eN(1-R) \alpha \eta \mu_0 \tau_1 F \quad (6)$$

We can assume one dominant transport path for the whole CPM spectral range for which the $\mu_0(E)$ is constant. In order to have $\tau_1(E) = \tau_1 = \text{constant}$, the quasi-Fermi levels must be stabilized. When we keep the photocurrent constant, and assume one dominant recombination center and one major type of carrier, both quasi-Fermi levels are stabilized [15]. This can also be interpreted by using the relation:

$$n = N_c \exp\{(E - E_{fn}) / K_B T\}$$

where n is the concentration of free electrons, E_{fn} is the quasi-Fermi level for electrons, and N_c is the density of

states at the band edge E_c , K_B is the Boltzmann factor, and T is the temperature. At room temperature, E_c and N_c are constant. If photocurrent is kept constant, n is a constant. Therefore the quasi-Fermi level is stabilized and the number of recombination centers does not change. So the same set of recombination centers governs the free carrier lifetime during the whole measurement. The free carrier lifetime, τ_1 , can be thought as a constant under the special condition mentioned above. For other parameters, $R(E)$ and η , $R(E)$ is a weak function of E and η is approximately equal to 1 in the temperature range from 150K to 300k [16]. So we can get:

$$\alpha_{cpm}(E) \approx \frac{\text{constant}}{N(E)} \quad (7)$$

where $N(E)$ is the number of photons necessary to keep $I_{s,ph}$ constant.

Since CPM measures only those transitions which contribute to the photocurrent, it only can "see" transitions which create mobile carriers. These transitions are labeled in Fig 3.1 as follows [14]: (a) from the valence band tail to the conduction band; (b) from the valence band to the conduction band tail; and (d) from defect states in the midgap to the conduction band. These transitions are the only ones which excite electrons to the conduction band, and are the relevant transitions to CPM because electrons dominate the photocurrent. In order to calibrate the relative α_{cpm} spectra

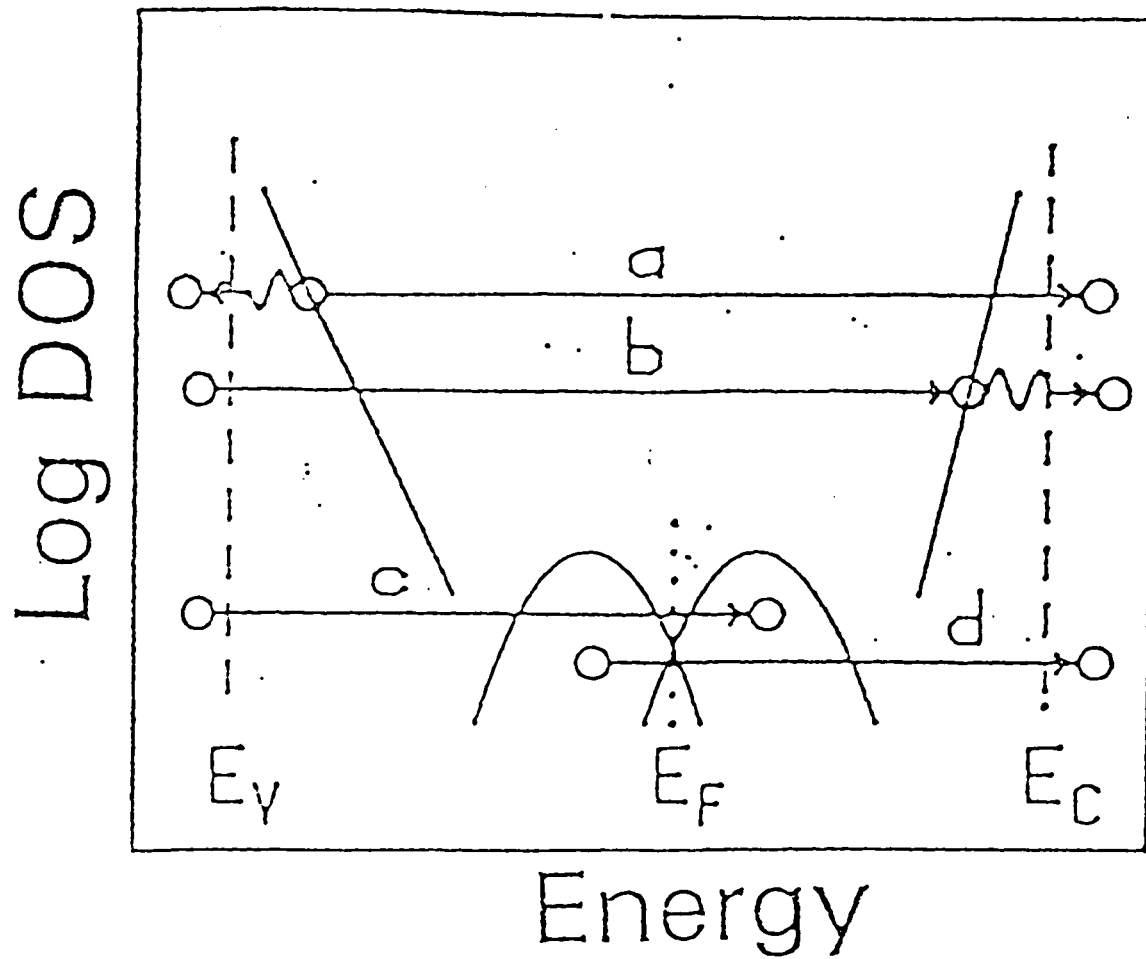


Figure 3.1
 Illustration of possible transitions in undoped
 a-Si:H. \rightarrow and \rightsquigarrow denote optical and thermal
 transitions, respectively.

to an absolute scale, we can match the CPM data to transmission results in the region above the energy gap (see the next chapter for details).

CHAPTER 4

EXPERIMENTAL SET-UP

Our experimental setup is shown in Fig.4.1. We use a lens to focus the light from a 200W Tungsten-halogen lamp on the slit of a PTI model-1307 monochromator. Various filters are used to cut off the higher order diffraction lines. The intensity of the light on the sample is controlled by adjusting the voltage for the power supply of the light source or using neutral density filters. The photocurrent is measured using a Keithley model-485 picoammeter and is kept constant at different wavelengths by changing the neutral density filters and the voltage of the power supply of the light source. After recording power supply voltage which is needed to keep the photocurrent constant at different wavelengths, the sample is replaced by a liquid nitrogen cooled Ge-detector. The intensity of light is then measured at corresponding voltages and wavelengths. The number of photons needed to keep the photocurrent constant is then calculated from the intensity of the light. In order to raise the sensitivity, a linear preamplifier is used with the detector.

The measurements are started at the long wavelength side, because the photocurrent is small due to lower absorption in this region. The intensity of light is varied until the ratio of photocurrent to dark current is above an order of magnitude at the longest wavelength (typically about 1459 nm). This

value of photocurrent is kept constant over the whole wavelength range (1459nm - 577nm) by changing the intensity of light or using neutral density filters. It is very important to allow to the photocurrent to stabilize before recording data.

In order to set relative CPM spectrum to the absolute scale, the optical transmission spectrum of the sample is measured by a double beam Perkin Elmer model UV-265 spectrophotometer. In order to account for substrate absorption, a Corning 7059 glass, which is the same as the substrate of the samples, was used as a reference in our measurements.

The absorbance coefficient A from the transmission measurement is defined as $\text{Log}(I_i/I_o) = A$, where the I_i and I_o are incident and transmitted light intensities, respectively. Using Lambert-Beer's law, we have $I_o = I_i \exp(-\alpha d)$. Solving these two equations for the absorption coefficient α yields:

$$\alpha = \frac{A \ln 10}{d} \quad (8)$$

where d is the thickness of the sample.

In our experiment, we used two samples which were prepared at the University of Kaiserslautern. These samples were prepared by the glow discharge technique at 250°C substrate temperature. The samples have two chromium electrodes with a spacing of 0.5mm. As can be seen from the

ratio of $\sigma_{\text{ph}}/\sigma_{\text{dark}}$ in Table 4.1, these films are device quality films.

Table 4.1 Sample Specifications

	Sample A	Sample B
Thickness in μm	2.0	1.14
$N_{\text{PH}_3}/N_{\text{SiH}_4}$	0	6.9%
$\sigma_{\text{Dark}} (\Omega^{-1}\text{cm}^{-1})$	6.33E-10	6.60E-7
$\sigma_{\text{Ph}} (\Omega^{-1}\text{cm}^{-1})$	3.02E-5	1.36E-3
$\sigma_{\text{Ph}}/\sigma_{\text{Dark}}$	4.77E4	2.06E3

CHAPTER 5

RESULTS AND DISCUSSION

In our experiment, the absorption spectra of two a-Si:H thin films are measured by the CPM method. The specifications of the samples are shown in Table 4.1. The effects of illumination and annealing on these samples are also investigated. Some important parameters, such as optical gap E_g , Urbach energy E_o , and dangling bond density N_s , are obtained from the CPM spectrum. The CPM spectrum is compared with the absorption spectrum obtained with Photothermal Deflection Spectroscopy (PDS) and the surface state density of defects N_{ss} is obtained.

Using equation (7), the absorption coefficient α_{cpm} for sample A and sample B is calculated in the energy region from 0.85eV to 2.15eV. After matching the spectra with transmission results, their CPM spectra are shown in the Figs.5.1 and 5.2. In the plots of $\log\alpha$ verses energy, the linear portions of the curves were used to obtain Urbach energy using equation (2). Fig.5.3 and 5.4 are the plots of $(\alpha E)^{1/2}$ versus energy for sample A and sample B, respectively. In these curves, best straight line fits were obtained in the energy region for which α is above 10^3 CM^{-1} . According to equation (1), the intercept with energy axis at $\alpha E=0$, gives the value of the band gap, E_g .

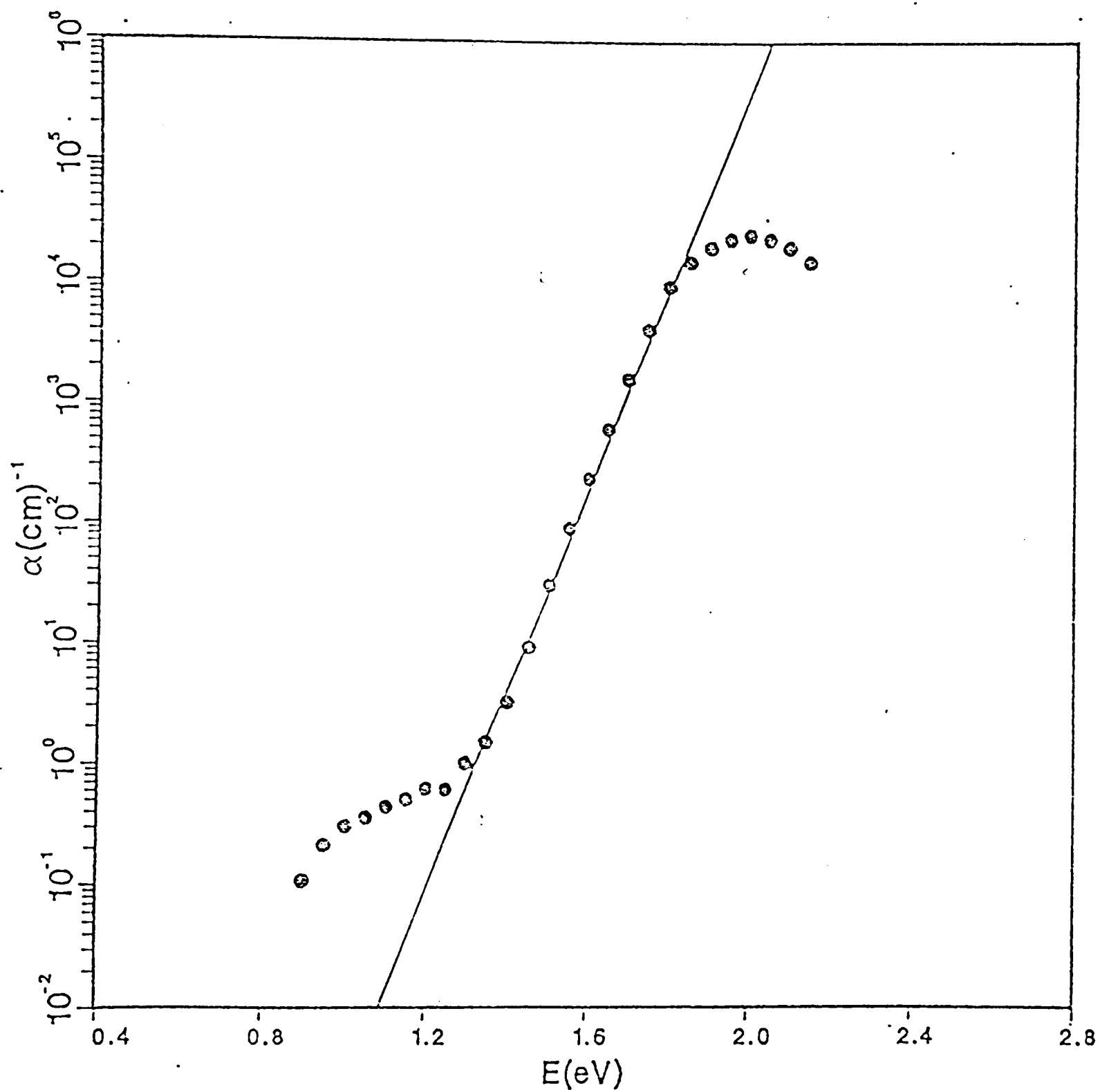


Figure 5.1

Absorption spectrum of sample A using CPM.

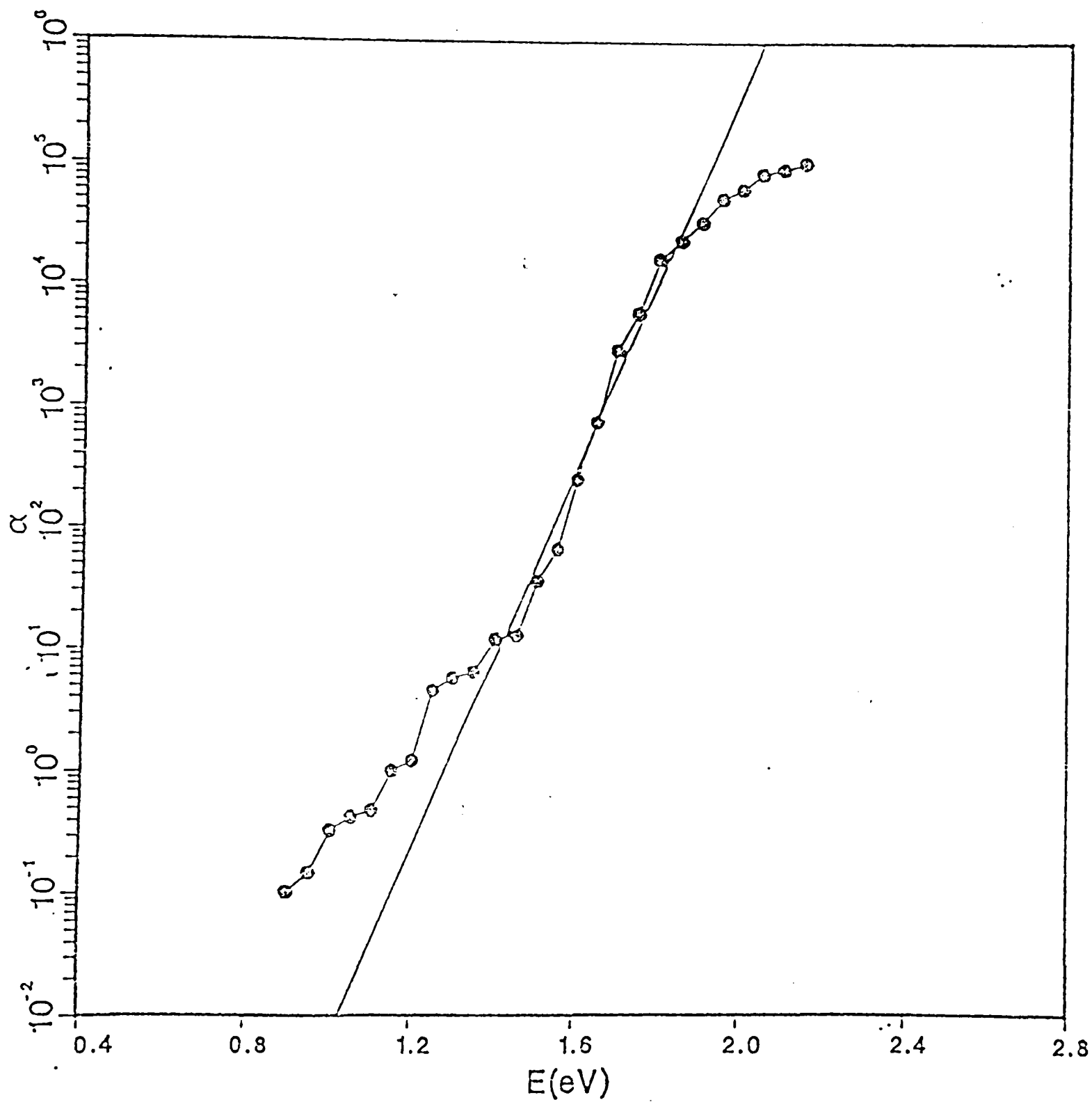


Figure 5.2

Absorption spectrum of sample B using CPM.

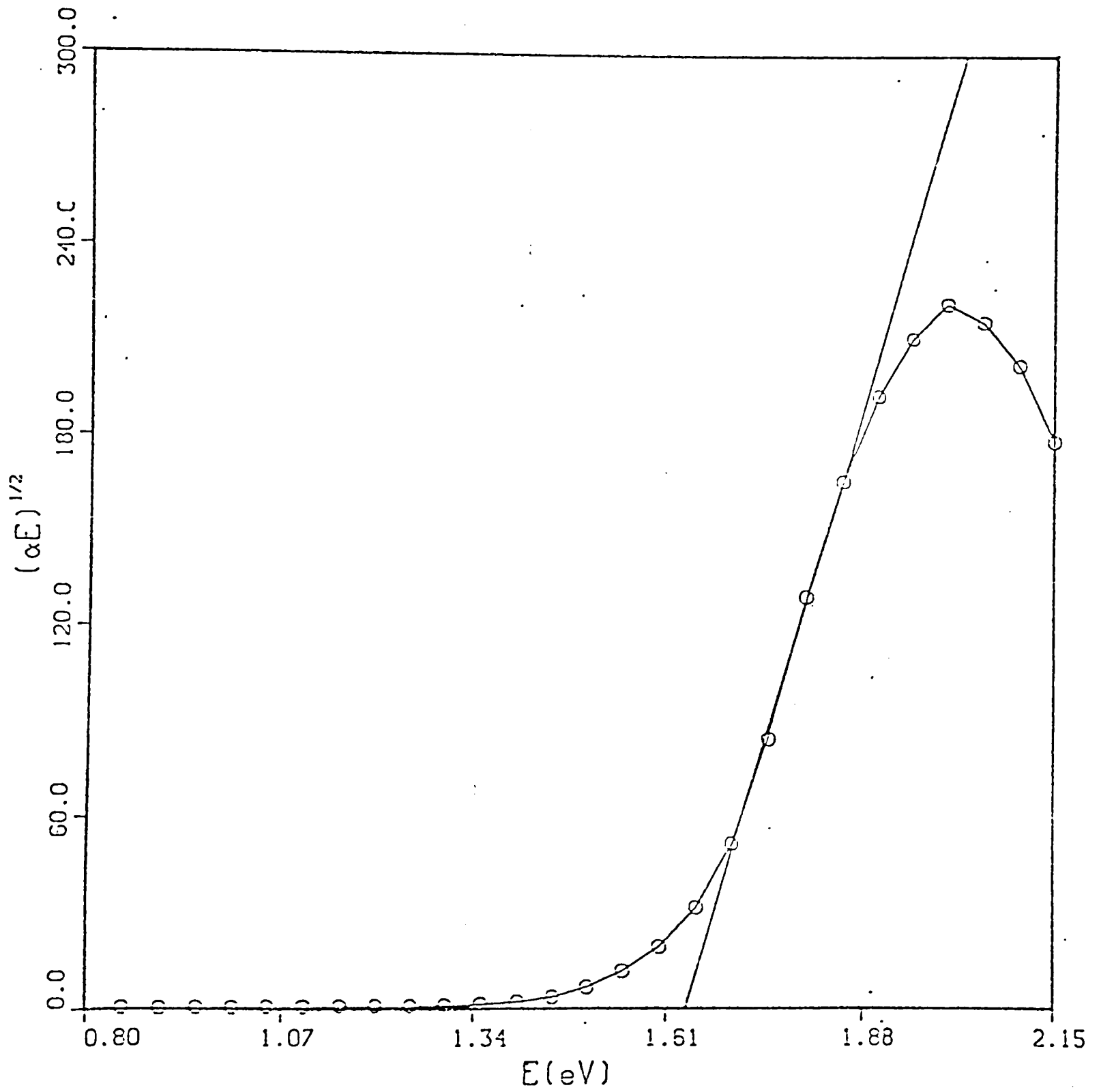


Figure 5.3

Square root of αE versus photon energy E for sample A.

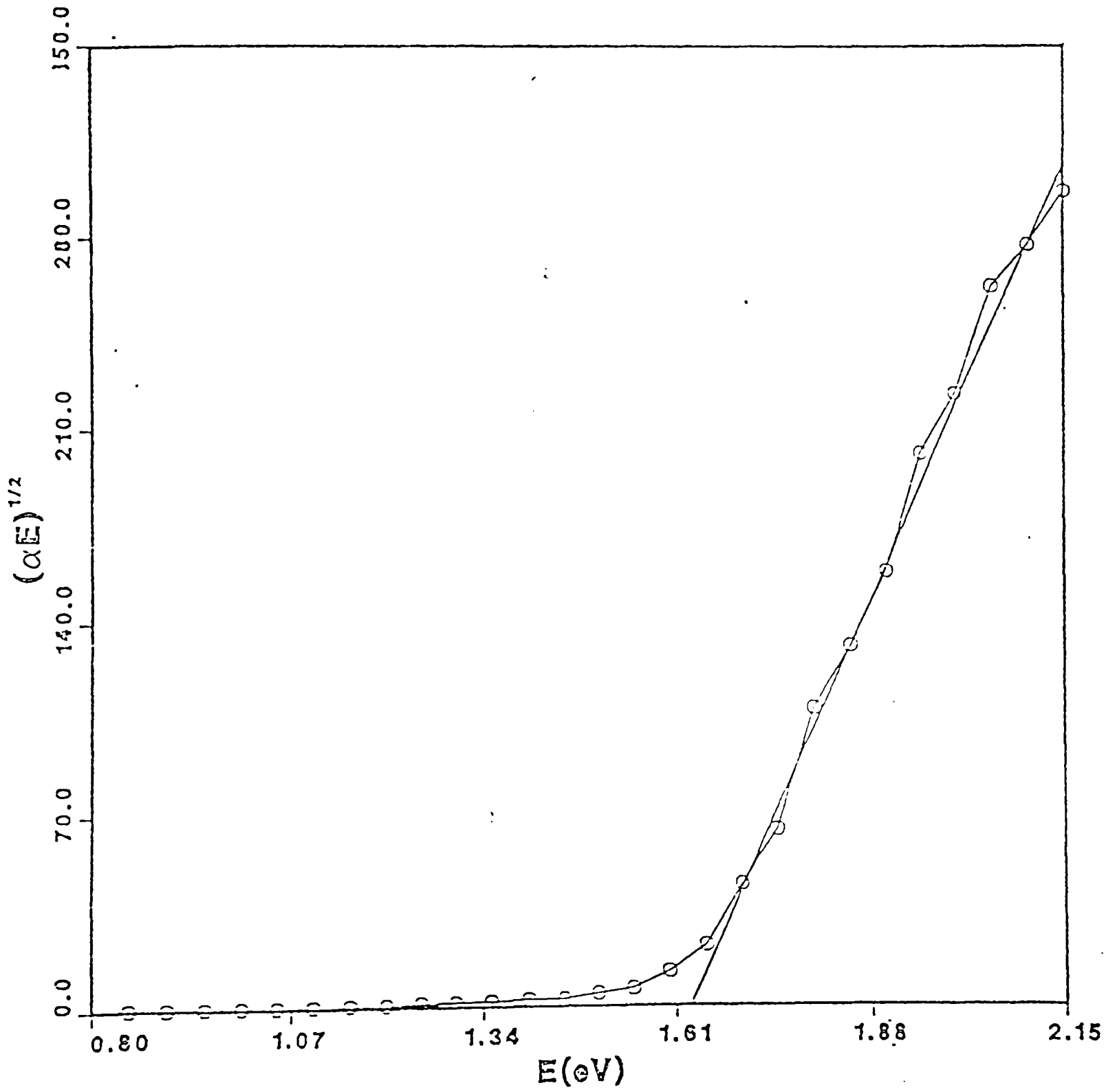


Figure 5.4

Square root of αE versus photon energy E for sample B.

Table 5.1 presents the optical band gap (E_g), Urbach energy (E_0) and the regression coefficients for the best fit of the data for sample A and sample B. The E_g and E_0 values for these samples are the typical values for good quality a-Si:H films.

Table 5.1

Optical gap and Urbach energy of sample A and sample B

	E_g (eV)	Regression Coef. of E_g	E_0 (eV)	Regression Coef. of E_0
Sample A	1.64 ± 0.005	0.938	$.053 \pm 0.0003$	0.997
Sample B	1.65 ± 0.004	0.990	$.054 \pm 0.0002$	0.983

Figure 5.5 compares the CPM and PDS spectra of sample A. The PDS spectra were measured at the University of Kaiserslautern. The shape of the CPM absorption curve is similar to the PDS curve with one important difference: the CPM absorption curve drops below the PDS curve at photon energies below the band gap. The main reason for this is that, when the photocurrent in the coplanar configuration of electrodes is carried through the sample, the contribution of a defective surface layer to the photocurrent is much smaller than that of the bulk in the region of low photon energy because of surface recombination [17]. Since CPM assumes absorption is inversely proportional to the intensity required to maintain constant photocurrent, the argument can be turned

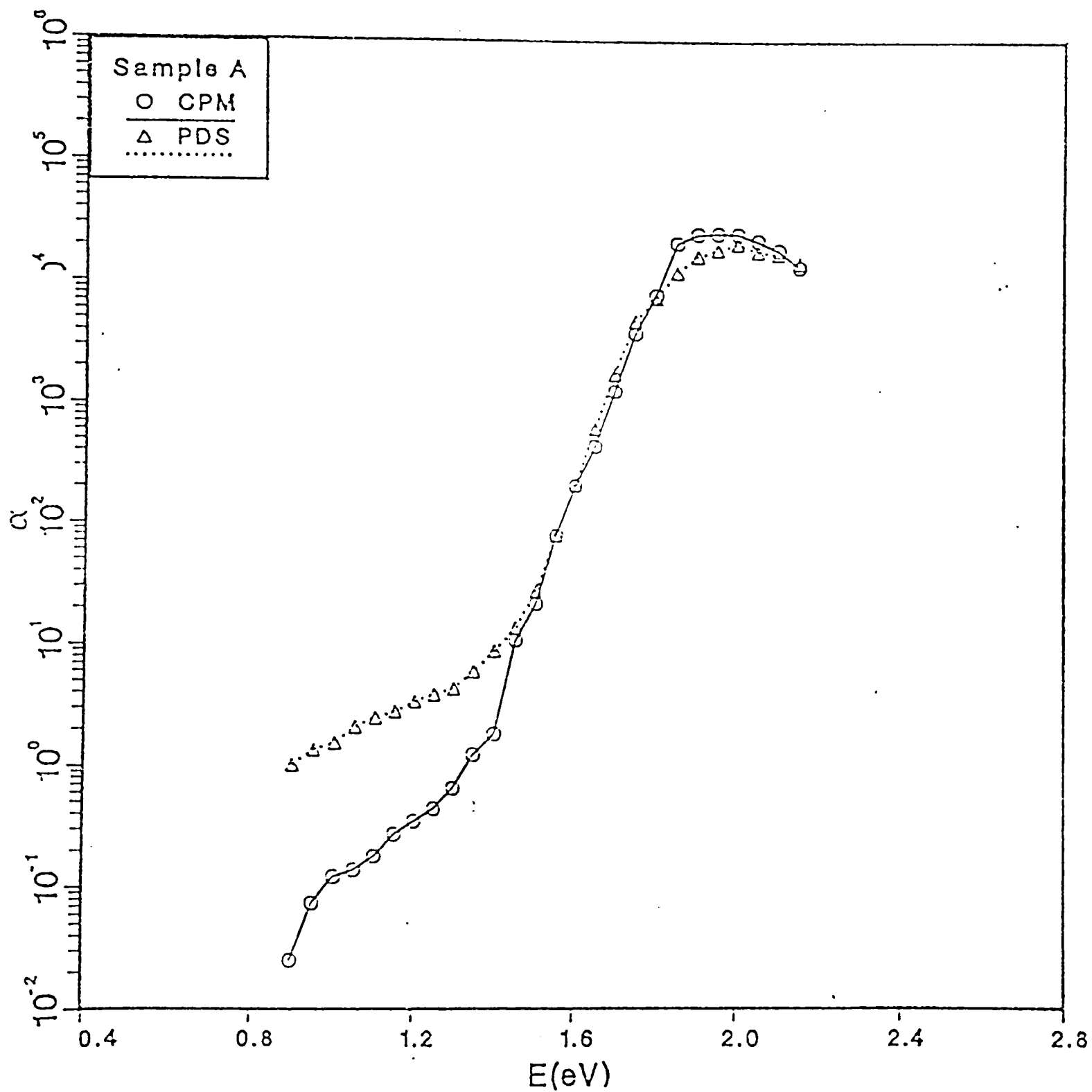


Figure 5.5
Comparison of absorption spectra of sample A using CPM
and PDS.

around: carriers generated near the surface have a reduced contribution to photocurrent and surface state absorption will hardly be seen at all in the region of low photon energy. This means CPM will be relatively insensitive to the surface. PDS is "all-seeing" in the sense that any level that can have an electron lifted in or out of it, whether it is at the surface or in the bulk, should be observable [2]. In general, the bands will be bent in the region near the surface, the direction of band bending at the exposed surface can depend critically on the nature of surface absorbance.

According to Jackson and Amer [10], the integral of this "excess" band-defect absorption should be proportional to the defect density. D.Slobodin compared CPM and ESR (Electron Spin Resonance) on glow discharge a-Si:H films, and modified the prefactor in equation (3) and yielded [2] :

$$N_s(\text{cm}^{-3}) = (1.9 \pm 0.3) \times 10^{16} \int \alpha_{cpm}(\text{cm}^{-1}) dE(\text{eV}) . \quad (9)$$

Using equation (9) and the Simpson integration method, the defect densities for sample A and sample B are $N_{s,A} = 9.3 \times 10^{15} \text{cm}^{-3}$ and $N_{s,B} = 3.4 \times 10^{17} \text{cm}^{-3}$, respectively. From our data, we find the defect density of sample B is more than one order higher than that of sample A. The main reason for this is the introduction of P-doping. As Stutzmann has pointed out that, doping of a-Si:H can lead to doping-induced changes of

the electronic density of states near the center of the band gap, i.e., changes in the density of deep defect levels [22].

Since CPM can only find the bulk defects and PDS can detect both the bulk and surface defects, equation (3) and (9) give us a general program for separating bulk and surface defect densities. Using the CPM spectrum and equation (9), one can find the bulk density, $N_{\text{def}}(\text{bulk})$, and use the PDS spectrum and equation (3) to give the bulk + surface defect density, $N_{\text{def}}(\text{effective})$. Then the surface density, N_{ss} , can be obtained by

$$N_{\text{ss}} = (N_{\text{s}}^{\text{eff}} - N_{\text{s}}^{\text{bulk}}) d \quad (10)$$

where d is the film thickness. From the PDS spectra, the defect densities for sample A and B are $N_{\text{s},\text{A}} = 1.8 \times 10^{16} \text{cm}^{-3}$ and $N_{\text{s},\text{B}} = 7.3 \times 10^{17} \text{cm}^{-3}$, respectively (the data are offered by the University of Kaiserslautern). By using equation (10), the surface densities for sample A and sample B, $N_{\text{ss},\text{A}}$, $N_{\text{ss},\text{B}}$ are $1.8 \times 10^{12} \text{cm}^{-2}$ and $4.4 \times 10^{13} \text{cm}^{-2}$, respectively. In order to find differences between the intrinsic and P-doped a-Si:H films conveniently, we list the data in Table 5.2 below:

Table 5.2

Defect densities of sample A and sample B

	Sample A	Sample B
N_s (bulk+surf.)	$1.8E16cm^{-3}$	$7.3E17cm^{-3}$
N_s (bulk)	$(9.26\pm.03)E16cm^{-3}$	$(3.44\pm.05)E17cm^{-3}$
N_{ss} (surf.)	$(1.75\pm.03)E12cm^{-2}$	$(4.40\pm.05)E13cm^{-2}$

In Fig.5.6, we show several absorption curves of sample A illuminated by Xenon arc lamp source for different exposure times at room temperature (the intensity of light is $100 \text{ mW}(cm)^{-2}$). From the Figure, we can find that these absorption curves do not change much except in the low energy region. Using Eq.2 and Eq.9, the Urbach energy E_0 and defect density N_s are obtained and shown in Table 5.3 below:

Table 5.3

Defect densities of sample A for different exposure times

Exposure Time	E_0 (eV)	N_s
1 HR.	$0.054\pm.0006$	$(1.91\pm.05)E16$
2 HR.	$0.055\pm.0003$	$(2.30\pm.03)E16$
3 HR.	$0.055\pm.0005$	$(2.84\pm.06)E16$
5 HR.	$0.055\pm.0003$	$(2.96\pm.04)E16$
10 HR.	$0.055\pm.0004$	$(3.04\pm.06)E16$

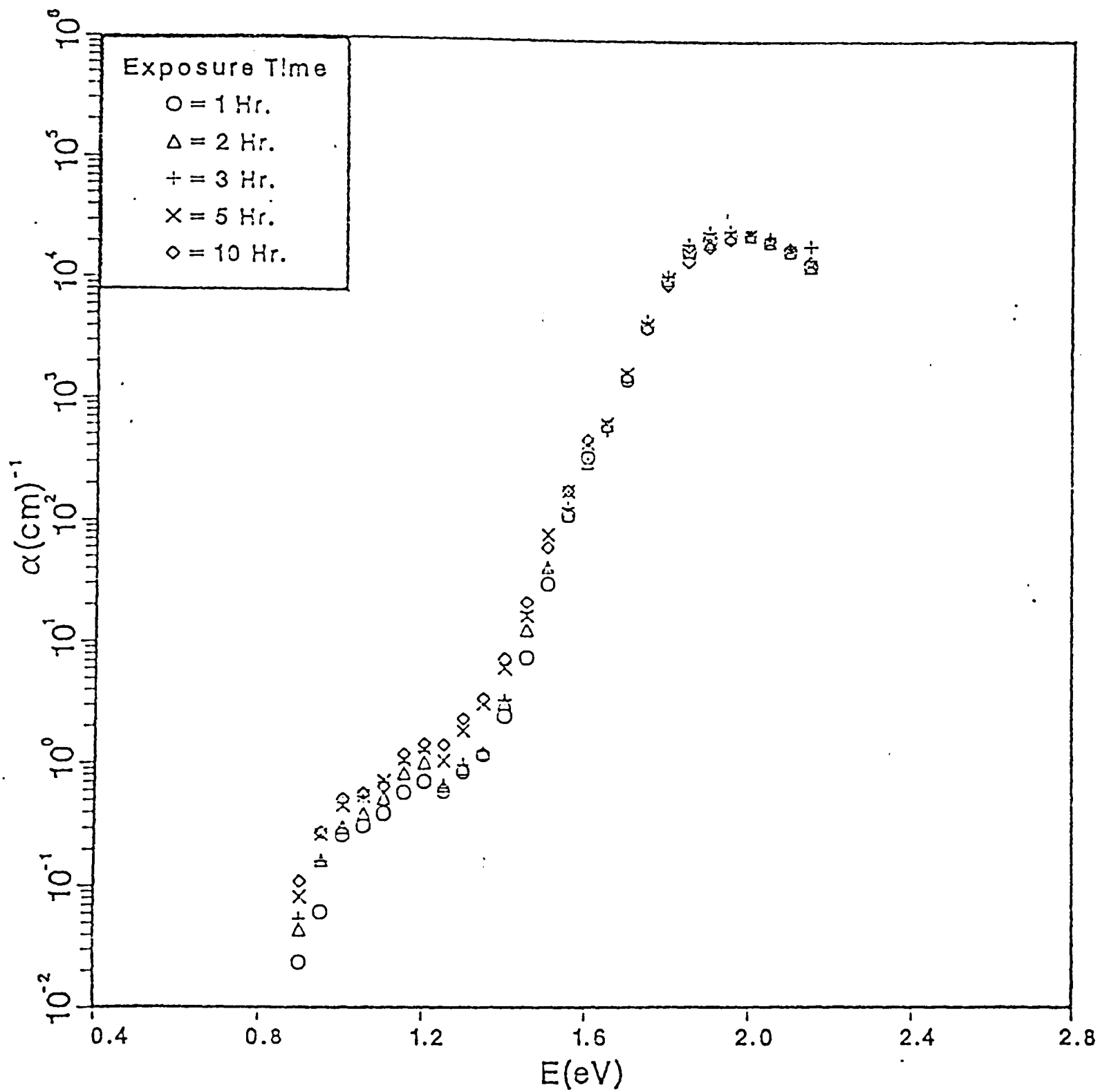


Figure 5.6
Absorption spectra of sample A after different exposure times to $100 \text{ mW}(\text{cm})^{-2}$.

From the table, we find that the Urbach energies change very slightly as the exposure time increases. The result is consistent with that from PDS [10]. In the region below 1.5 eV, the absorption curves move up as the exposure time increases. The phenomenon shows the defect creation which is mainly related to the increase of the number of dangling bonds. From the change of defect densities at different exposure time, we can find the rate of defect creation is not linear. Although the rate of defect creation goes down after 3 hours exposure, there is still no sign to show saturation or reach a steady state. By fitting the time dependence of defect density N_s , we find that the defect density N_s increases as a function of time, $N_s(t) \propto t^{0.29}$. From experimentally observed creation of additional Si dangling bonds, we can make two plausible deductions. The first is that the weak Si-Si bonds are broken as a consequence of illumination. The Si-H bonding energy is too high (3.5 eV) [19] for bond breaking to occur at photon energies as low as 1.5 eV. The second is the Staebler-Wronski effect is predominantly a bulk effect, because the CPM deduced subgap α is only bulk controlled.

In Fig.5.7, we compare the absorption spectrum of sample A after annealing for 1 hour at temperature 200C° in dark with the absorption spectrum after 10 hours exposure at 100 mW/cm² (room temperature). Some parameters of sample A which are derived from the spectra are compared with the initial state of the sample as shown in Table 5.4 below:

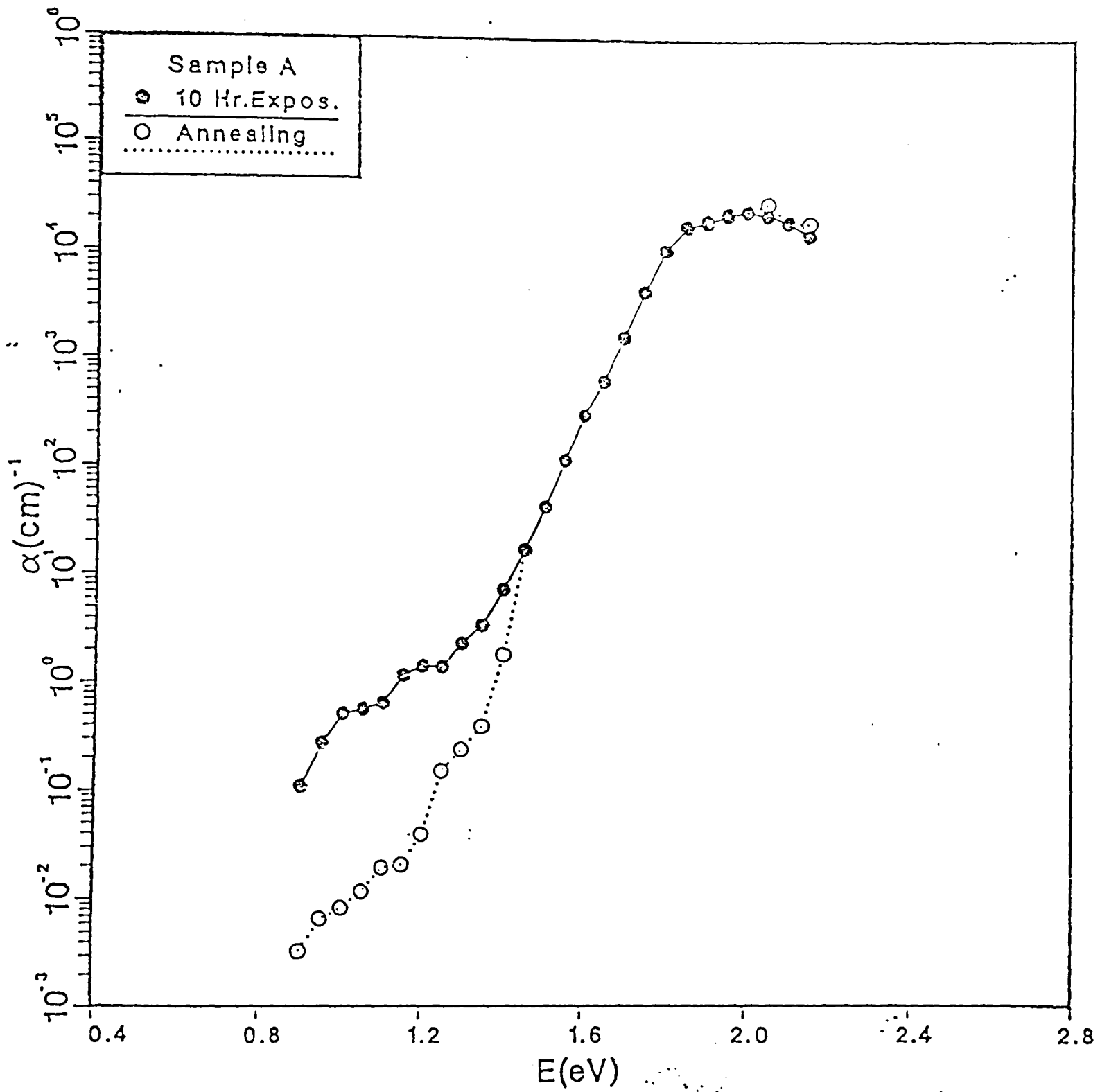


Figure 5.7

Comparison of absorption spectra of sample A after 1 hr. annealing at 200°C in dark and after 10 hr. exposure to 100 mW/cm².

Table 5.4

Comparison of E_g , E_o and N_s of initial state of sample A with those after 10 hr. exposure and 1 hr. annealing

Sample A	E_g	E_o	N_s
Initial	1.64 ± 0.005	0.054 ± 0.0003	$(9.26 \pm 0.04) E15$
10 Hr. Exp. (100mW/cm ²)	1.64 ± 0.002	0.055 ± 0.0004	$(3.04 \pm 0.06) E16$
Annealing (200C ^o)	1.64 ± 0.003	0.055 ± 0.0004	$(8.20 \pm 0.03) E15$

The spectra and data show a clear and reproducible enhancement in gap-state absorption after illumination. Annealing at 200C^o reduces the density below the initial value indicating that the initial state of the sample was not the deposited condition. It also indicates that the created defects have been eliminated due to annealing.

CHAPTER 6

CONCLUSIONS

We have used CPM to obtain the absorption spectra for both undoped and phosphorus-doped a-Si:H films. The optical gap, E_g , Urbach energy, E_o , and defect density, N_s , are obtained from the analysis of the spectra. Comparing our data (initial state) with the results from PDS for undoped sample A and P-doped sample B, we find the magnitude of E_g and E_o are nearly the same except the defect density N_s (they are shown in the appendix). As discussed previously, the reason is that these two methods have different sensitivities for the surface and bulk of the films and detect different transitions in the low energy region. From the experimental description and the results, we can also find that the CPM is a sensitive and efficient tool for studying thin films of a-Si:H.

In the study of light induced metastability of a-Si:H, we have found that the increase in the density of dangling bonds is nonlinear. It obeys a power law with an exponent of 0.29 of the illumination time. The result is in good agreement with the literature. For the creation of additional Si dangling bonds at different illumination times, we have found, that in the energy region below 1.5 eV, the absorption curves move up. This means that the defect density increases as the illumination time increases at constant temperature. In this situation, all of energy to cause the creation of defects is

supplied by the light excitation. So, we can make the deduction from the experimentally observed creation of additional Si dangling bonds: the weak Si-Si bonds break in the sample. Since the effect seems to be intrinsic to the pure a-Si:H network, it can only involve the breaking of Si-H or Si-Si bonds. Breaking of the Si-H bond requires an energy 3.5eV and can occur when a Si:H is irradiated with energetic particles [20], or when the material is annealed at temperatures above 400°C [21]. So, when the photon energy is as low as 1.5eV, the only possibility is the breaking of the weak Si-Si bond. We have also found that the density of light induced defects can return to its original value by annealing at 200°C in dark. Since the CPM method is insensitive to the surface in low energy region, we think the metastability results predominantly from a bulk effect.

There is a lot of scope for further research in this area. For instance, our work concentrates only on the creation of defects which result from the white light, but the relation between the photon energy (different wavelength) and the rate of creation of defects is not known. Although we think the Staebler-Wronski effect is predominantly the bulk effect, the effect and mechanism from the surface under illumination is still not known exactly. Although we can explain the S-W effect by using the potential well model, some basic facts, such as whether hydrogen is directly involved in the reversible process, still remain to be decided experimentally.

So, we think there is still much work needed to do for understanding the promising material.

REFERENCES

1. R.A.Street, Hydrogenated Amorphous Silicon, Cambridge University Press, New York, 1991.
2. Z.E.Smith, V.Chu, k.Sphepard, S.Alishi, D.Slobodin and S.Wanger, Appl. phys.. Lett. 50, 21, 1987.
3. Arun Madad and Melvin P.Shaw, the Physics and Application of Amorphous Semiconductors, Academic Press, Inc., Boston, 1988.
4. H.Fritzsche, Optical Effect in Amorphous Semiconductors, AIP Press, New York, 1984.
5. S.C.Moss. and J.F.Graczyk, Proc. Int. Conf. Phys.Semicond. 10th, 1970.
6. Tasi C.C. Amorphous Silicon and Related Materials, World Scientific Inc., New Jersey, 1988.
7. G.D.Cody, the Optical Absorption Edge of a-Si:H, Academic Press Inc., Florida, 1984.
8. M.Janai, R.Weil, H.K. Levin, Appl. Phys. 52, 3622, 1981.
9. F.Urbach, Phys.Rev. 92, 1324, 1958.
10. Nabil M. Amer and W.B.Jackson in a-Si:h, Academic Press Inc. Florida, 1984.
11. M.Stutzmann, W.B.Jackson and C.C.Tasi, Phys.Rev. B32, 23. 1985.
12. M.Stutzmann, W.B.Jackson and C.C Tasi, Phys.Rev. B34, 63, 1986.
14. J.Kocka, M.Vaecek and A.Triska, Energy and Density of Gap States in a-Si:H, World Scientific Publishing Company, New Jersey, 1988.
15. K.Pierz, B.Hilgenberg and G.Weiser, J. of Non-Cryst. Solid. 97/98, 63, 1987.
16. F.Carasco, E.W.Spear, Phil. Mag. B47 NO.5, 495,1983.
17. M.Vanecek, J.Kocka, J.Stuchlik and A.Triska, Solid. Comm. Vol.39, 1199, 1981.
18. J.David Cohen and M.L.Tomas, Part 4, Amorphous Silicon Material and Solar Cells, Denver, 1991.

19. K.Zellama, P.Germain, and S.Squelard J.Non-Cryst. Solid. 35/36, 225,1980.
20. W.M.Pontuschka, W.W.Carlors, P.G. Tylor, Phys. Rev. B25, 4326,1982.
21. D.K.Biegelsen, R.A.Street, and C.C.Tasi, Phys.Rev. B20, 4839, 1979.
22. M.Stutzmann, D.K.Biegelsen, and R.A.Street, Phys. B15, 5666, 1987.

APPENDIX

Some parameters of sample A and sample B (initial state) are shown in Table A.1 and Table A.2. The data of PDS are from the University of Kaiserslautern.

Table A.1

Comparison of E_g , E_o , and N_s of initial state of sample A using CPM and PDS

Sample A	E_g	E_o	N_s
CPM	$1.65 \pm .005$	$0.053 \pm .003$	$(9.26 \pm .04) E15$
PDS	1.65	0.0524	1.8E16

Table A.2

Comparison of E_g , E_o and N_s of initial state of sample B using CPM and PDS

Sample B	E_g	E_o	N_s
CPM	$1.65 \pm .004$	$0.054 \pm .002$	$(3.44 \pm .06) E17$
PDS	1.65	0.0551	7.3E17